SLAC–PUB–7887
July 1998

Results from the *BABAR* Electromagnetic Calorimeter Beam Test

Roger J. Barlow[1], Roland Bernet[2], Christopher K. Bowdery[3], Jens Brose[4], Theresa Champion[5], Gerd Dahlinger[4,6], Paul Dauncey[7], Peter Eckstein[4], Gerald Eigen[8], Dietrich Freytag[9], John Fry[6], Neil I. Geddes[7], Stanley S. Hertzbach[10], Vladimir Ivanchenko[11], Colin Jessop[9], Damian Johnson[12], Mary King[9], Eckart Lorenz[13], Helmut Marsiske[9], Steve McMahon[6], Howard Nicholson[14], Jim Reidy[15], Rafe Schindler[9], Klaus R. Schubert[4], Rainer Schwierz[4], Iain Scott[12], Reiner Seitz[4], Zurab Silagadze[11], Bernhard Spaan[4], David P. Stoker[16], Edward Tetteh-Lartey[12], Roland Waldi[4,†], William J. Wisniewski[9], Craig R. Wuest[17]

---

† Corresponding author. E-mail Waldi@physik.tu-dresden.de

1 University of Manchester, Manchester, UK
2 University of Edinburgh, Edinburgh, UK
3 University of Lancaster, Lancaster, UK
4 Technische Universität Dresden, Dresden, Germany
5 Brunel University, London, UK
6 University of Liverpool, Liverpool, UK
7 Rutherford Appleton Laboratories, Chilton, Didcot, UK
8 University of Bergen, Bergen, Norway
9 Stanford Linear Accelerator Center, Stanford University, Stanford, California, USA
10 University of Massachusetts, Amherst, Massachusetts USA
11 Budker Institute of Nuclear Physics, Novosibirsk, Russia
12 University of London, Royal Holloway and Bedford New College, Surrey, UK
13 Max Planck Institut für Physik, Munich, Germany
14 Mount Holyoke College, South Hadley, Massachusetts USA
15 University of Mississippi, Oxford, Mississippi, USA
16 University of California, Irvine, California, USA
17 Lawrence Livermore National Laboratory, Livermore, California, USA

Submitted to Nuclear Instr. and Meth. A

Abstract

We present results from the PSI test beam run for the electromagnetic calorimeter of the *BABAR* experiment. A system of 25 CsI(Tl) crystals was tested with electrons and pions in the momentum range from 100 to 405 MeV/c. Results are presented on crystal light output, on coherent and incoherent noise, on energy resolution and on spatial resolution. The design energy resolution of the Technical Design Report of *BABAR* were achieved.

1 Introduction

The observation of CP violation in B meson decays as predicted by the Standard Model motivates the construction of B meson factories. One of these is PEP II, which was approved in 1993, and is currently being built at SLAC. It is an asymmetric e^+e^- collider, with a low energy positron beam of 3.1 GeV and a high energy electron beam of 9 GeV. Thus, $B\overline{B}$ pairs are produced from $\Upsilon(4S)$ decays with a boost of $\beta\gamma = 0.56$ in the beam direction, and their lifetime difference can be measured from their vertex positions along the beam axis.

The e^+e^- annihilation events are registered by the detector *BABAR* [1], a universal spectrometer featuring a silicon vertex detector, surrounded by a cylindrical drift chamber, followed in radial direction by a Cherenkov imaging device (DIRC), a CsI calorimeter, a superconducting magnet coil and an instrumented flux return (IFR).

Electromagnetic calorimetry is essential for the success of the *BABAR* experiment, and challenging performance goals have been set [1]. As part of the process of designing and building a CsI(Tl) calorimeter to meet these requirements, a system of 25 crystals was operated in a testbeam, as a small scale version of the final detector of 6580 crystals. This testbeam run aimed to obtain results needed for the design of the calorimeter system, to make measurements to validate the Monte Carlo, and to start the learning process of operating and calibrating a CsI Calorimeter. Specific objectives were to study energy resolution, spatial resolution, effects of staggering and gaps, and hadronic showers.

1.1 The PSI Beam

The tests were performed in the $\pi M1$ beam at the Paul Scherrer Institute [2] which provides a mixture of particles with beam momentum selectable between 100 and 500 MeV/c.

This momentum region was chosen because the photon spectrum in the *BABAR* experiment will peak in this region. Furthermore, the resolution at these low momenta/energies is sensitive to effects such as coherent noise which are hard to understand and to evaluate on a bench or by simulations.

The beam momentum spread is given as 0.1% FWHM[2]. Particle identification is possible from the time of flight of the particles over the 20.6 m

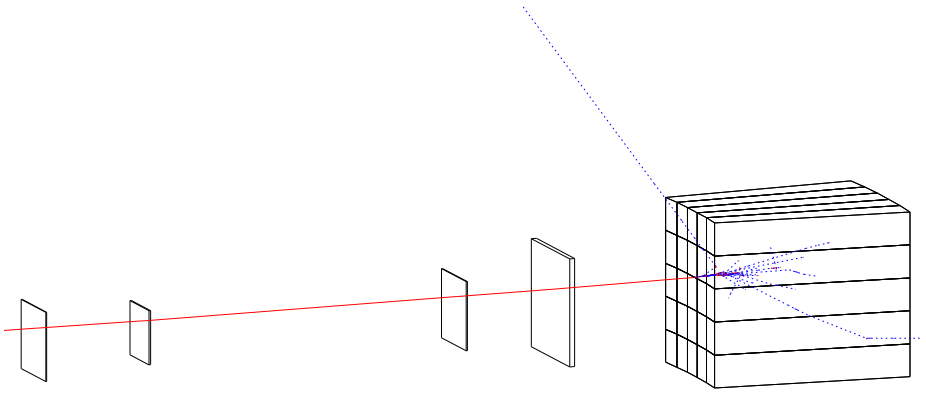

Figure 1: The experimental configuration. A Monte Carlo simulation is shown of an electron passing through the first set of wire chambers, the small scintillator, the second wire chambers, and the large scintillator, before showering in the crystal matrix.

path from the target to the experimental area, determined by comparing the arrival time measured by the trigger scintillators in front of the crystal matrix with the 20 ns time structure of the beam.

We used the beam in parallel mode; it had a very small angular divergence, and a transverse size of some tens of centimeters; this size, and the beam profile, varied considerably with beam momenta.

1.2 The Calorimeter Setup

25 CsI(Tl) crystals, produced by the Institute for Single Crystals, Kharkov (Ukraine), were used. Each one was 36 cm long and tapered in one dimension, measuring $6 \times 6\,\mathrm{cm}^2$ at the rear face and $6 \times 5\,\mathrm{cm}^2$ at the front.

Each crystal is wrapped and equipped with a readout system as described in the following section, and protected by a housing of $300\,\mu$m Kevlar walls with open ends. These 25 units were arranged in a 5 by 5 matrix with the parallel sides in the horizontal direction.

For the analyses described here, the crystals were stacked with the front faces flush, and the beam direction parallel to the gap between the 3rd and 4th columns of crystals, as shown in Fig. 1.

The crystals were enclosed in a light-tight and RF tight environmental box. A cooling system kept the temperature stable at 18°C within 1°C,

except when the box was opened for access. It proved harder to control the humidity, however this did not result in any adverse effects.

The entire matrix and box were mounted on a turntable and could be rotated. Data were taken at several angles and were also taken with the crystals in a staggered configuration, similar to the end of the barrel calorimeter in *BABAR*.

The position and direction of the beam particles was measured by two planes of multiwire proportional chambers. Timing was provided by scintillators, which were also used in the trigger. The scintillators were moved upstream of the wire chambers in the later runs, in order to reduce the effect of multiple scattering on the position and direction measurements.

1.3 Electronics

Crystals were read out at the back by two photodiodes as described in section 2 below. Signals from the two diodes were amplified and shaped separately by a dual range preamplifier mounted at the rear end of each crystal. These P196 preamplifiers [3], constructed at SLAC, are similar, but not identical, to those to be used in the final *BABAR* detector. Signals from the preamplifiers were connected through a panel on the environmental box to a set of receiver boards. These routed the signals to the voltage sensing SLAC 12 bit ADC units of type ADC-32 in the control room which measures the voltage at the peak of the shaped pulse. One bit in the ADC corresponded to about 80 keV of energy deposited in the high gain preamplifier channels, and 2 MeV for the low gain channels.

This combination was also used to form a 'pre-veto' 20 μsec inhibiting gate, to ensure that a trigger did not occur soon after another beam particle had hit the matrix. This is a sufficiently long time for the scintillation light to have diminished to a negligible level. However, it turned out to be not long enough to avoid undershoots from the AC coupling of the preamplifier.

The electronics gains were calibrated by injecting pulses from a DAC into the preamplifiers during short dedicated calibration runs. Electronics calibration was also monitored by the DAQ software: every 3 minutes a pedestal run of 100 events was taken with the trigger logic inverted such that no beam particle had hit the calorimeter.

The data acquisition system and the trigger are described in ref. [4].

1.4 The Run Schedule

All 25 crystals were first individually calibrated with electrons in the beam using a large scintillator between the wire chambers and two crossed finger scintillators in front of the crystals. The matrix of 25 was then assembled, and data were taken at various beam momenta and box angles. The central 9 crystals were then recalibrated to check the stability, which turned out to have slightly changed, as will be discussed in section 3. Further measurements were then taken with different crystal configurations.

Data were taken at momenta of $100, 135, 215, 320$, and $405\,\mathrm{MeV}/c$, mostly with negative beams containing e^-, π^-, and μ^- particles. The fractions of different particles varied strongly with beam momentum. Some runs at $405\,\mathrm{MeV}/c$ were taken with positively charged particles, which included protons. Data were recorded in runs of 200,000 events, which took 2 to 5 hours to accumulate, and written to exabyte tapes for later offline analysis [5].

2 Light Output

2.1 Crystal Light Collection

13 crystals were equipped with direct readout and 12 crystals with wavelength shifter, in order to compare the performance of the different setups. The 13 crystals were equipped [6] with two $20 \times 10\,\mathrm{mm}^2$ Hamamatsu S 2744-08 photodiodes, with a Silicon Nitride upper layer. These were glued on a 2 mm thick lucite plate with a surface area matched to the crystal rear face, which was pressed onto the back of the crystal. This arrangement of two diodes gives typically (6600 ± 400) photoelectrons / MeV [7]. An optical grease coupling between the plate and the crystal was used in later runs. This gives about 20% more light [6, 8], though it was feared that this could lead to Thallium diffusion processes degrading the performance of coupling medium and crystals during the time of running the test experiment.

The readout of the remaining 12 crystals consisted of a 3 mm thick wavelength shifter (surface area $5 \times 5\,\mathrm{cm}^2$) with two $30 \times 3\,\mathrm{mm}^2$ active area photodiodes (Hamamatsu S 3588-03 model 5400) glued on adjacent lateral faces. The wavelength shifter consisted of a lucite carrier doped with a fluorescent dye. This dye has its absorption maximum at 550 nm, well matched to the emission peak of CsI(Tl), and re-emits light at 640 nm where the quan-

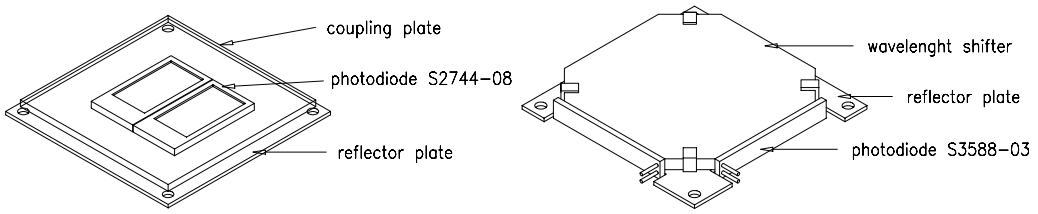

Figure 2: The two readout setups described in the text: direct readout with two diodes (left, the transparent lucite coupling plate is glued on top of the diodes) and wavelength shifter with two diodes at adjacent sides (right). The top sides of both setups face the crystal.

tum efficiency of the photodiode is about 15% higher than at 550 nm. The wavelength shifter was coupled to the crystal via a 1 mm airgap. The photoelectron yield has been determined using the same crystals as in the previous measurements, resulting in (6000 ± 300) photoelectrons / MeV [6].

For both readout options, a diffuse white reflector was located behind the lucite plates. The two readout schemes are sketched in Fig. 2. All crystals were wrapped with two layers of 160 μm thick Tyvek polyethylene fleece 1056D plus one layer of 5 μm aluminized Mylar.

2.2 Preliminary Measurements

The lightyield of all crystals was measured in a bench setup at Dresden before shipping to PSI. The apparatus used [7, 9] consisted of an extended-red sensitive photomultiplier tube Hamamatsu R669 coupled via an airgap to the crystal rear inside a light-tight aluminum box. The spectral range of the multialkali photocathode is well matched to the emission spectrum of CsI(Tl). The uniformity of the light yield along the crystal was determined by measuring pulse height spectra of a ^{137}Cs source (γ energy 662 keV). The source was located behind a 10 cm diameter lead collimator with a 6 mm thick channel. The collimator was moved along the crystal in steps of 2 cm. A scan took typically 30 minutes. During this time gain variations were monitored by measuring the light yield from α particles from a ^{241}Am source fixed at the crystal surface. The gain corrected ^{137}Cs photopeak position served as a measure of the light yield. If the RMS non-uniformity along the crystal exceeded 2% of the average pulse height, the crystal was tuned by putting an appropriate black strip on the wrapping material, thus reducing the light

yield locally. The relative light yields of different crystals were determined by averaging over the crystal length and comparing to a standard one cubic inch crystal measured with the same readout setup. After the tuning procedure all crystals showed a non-uniformity below 2% (RMS). Their average light yield was $(69 \pm 7)\%$ (RMS) compared to the standard crystal.

In order to determine the photoelectron yield per γ energy, the response of the readout chain with respect to the charge produced in the photodiode has to be known. Therefore an ^{241}Am source, emitting γ rays of 59.5 keV, was placed directly onto the entrance window of the photodiode. Those photons, when absorbed in the silicon layer of the diode, produce one electron-hole pair per 3.61 eV, thus providing a tool to determine the absolute gain of the electronics. From a subsequent determination of the photopeak of a ^{88}Y source (1836 MeV γ) placed at the crystal front face, the absolute photoelectron yield with photodiode readout can be derived. The photodiodes were read out by a charge sensitive Canberra 2003 T preamplifier. After amplification each signal was fed into a spectroscopic shaping amplifier (Canberra AFT 2025, 2 μs shaping time) and analyzed with a peak sensitive ADC [7]. The light yields varied between 5700 and 7000 photoelectrons / MeV for the 25 crystals.

2.3 Measurements at the Testbeam

At PSI, a much lower light yield was observed. A detailed analysis taking into account the calibration constants (see section 3), the electronics gain as measured in electronic calibration runs, and simultaneous ^{241}Am 59.5 keV γ reference measurements allowed us to determine the photoelectron yield at the beamtest. It was about 3200 photoelectrons / MeV both for direct and wavelength shifter readout with variations of about 15% between different crystals. These values were verified after the beamtest in lab measurements using this setup.

From an analysis in the lab, different reasons for the degradation of the light yield were found. The P196 preamplifiers were mounted in a small readout box on the crystal rear. The mechanical design of this readout box resulted in different light coupling and reflecting properties compared to the lab measurements. The short time-scale for preparation of the beamtest did not allow for the final readout boxes. For direct readout, the changes in the reflecting properties (holes and screws in the reflecting plate behind the

photodiodes, different distance of the reflector to the crystal surface) and coupling properties (airgaps between crystal and coupling plate because of its non-planar surface) reduced the photoelectron yield to about 62% of the values measured in the previous lab setup. For mechanical reasons the surface area of the wavelength shifter used at PSI was reduced by 30% leading to a light yield loss of similar order of magnitude. The different shaping times of P196 resulted in an additional reduction of photoelectron yields of about 15% for both readout options.

These degradations explain the light losses in the testbeam setup and were later recovered in lab measurements by appropriate changes of the setup leading to the final design of the *BABAR* readout box. A more detailed description is given in ref. [10].

3 Calibration Procedures

The calorimeter performance characteristics presented in this note are based on a three step calibration procedure. An initial gain calibration was performed for all crystals using electrons. Drifts in the gain calibration of $\pm 2\%$ and pedestal variations observed during the course of the 18 day test period are corrected run-by-run. Regular pedestal runs, used to track short term pedestal variations, are used off-line to define dynamic pedestals for each channel. A calibration procedure based on the energy loss of charged pions can be performed for the subsample of the 9 central crystals. In addition the linearity of the electronics has been checked at regular intervals using an electronic pulser system.

3.1 Initial Electron Calibration

Prior to the construction of the 5×5 crystal matrix each crystal was individually calibrated. The calibration was performed using 215 MeV/c electrons at normal incidence to, and impacting the central region of, the front face of the crystal. The impact point was restricted to an area of $\sim 1 \times 1$ cm^2 by means of a special trigger using a pair of crossed finger counters in front of the crystal. Monte-Carlo simulations of electrons, traced through the entire beam path before hitting the crystal, indicate that at 215 MeV/c the most probable energy deposition in a single crystal is 80.5% of the beam energy.

For each diode, both for low gain and high gain channels, the relationship between the most probable number of pedestal subtracted ADC counts and energy deposited in a crystal is determined by fitting the data with a four parameter fit to a logarithmic normal distribution [11].

Typical calibration constants (see section 5 for details) of $C_E^H \approx 80$ keV per ADC channel for the high gain output and $C_E^L \approx 2$ MeV per ADC channel for the low gain output were obtained. Figure 3 shows the distribution of the calibration constants for the low gain and high gain channels separately.

We assume that the relationship between ADC counts and energy, determined at 215 MeV/c, is linear over the range from 1 to 325 MeV. The lower limit of 1.0 MeV is defined by the typical single crystal energy threshold of 1.5 times the mean equivalent noise energy (see section 4) and 325 MeV corresponds to 80.5% of the maximum beam energy. This assumption relies

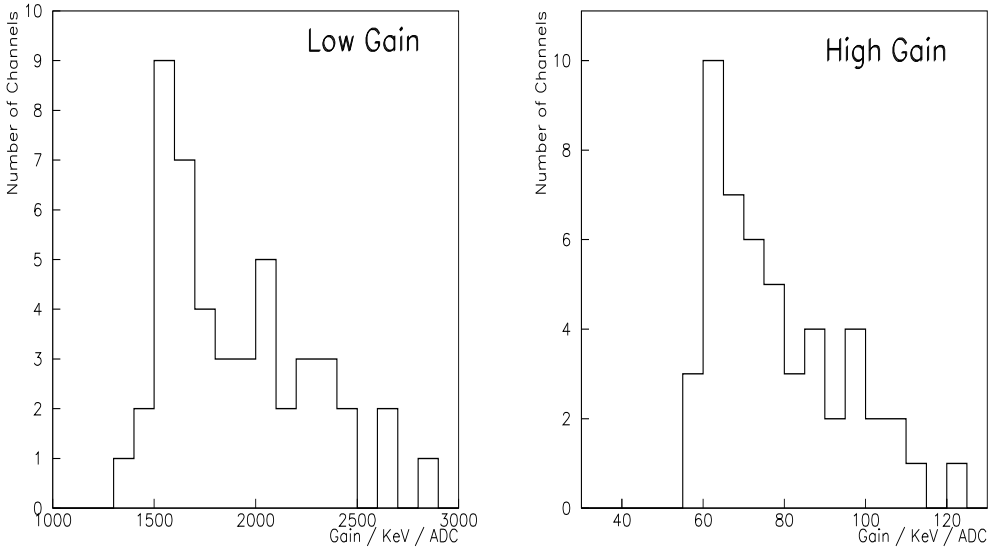

Figure 3: Distribution of the calibration constants for the (a) low gain channels and (b) the high gain channels

on the linearity of the light yield with energy and linearity of the electronics gain. We have checked the latter by injecting a range of known charges directly into the individual preamplifiers.

3.2 Electronics Gain

Each preamplifier includes a coupling capacitor in parallel to the photodiodes. By sending a pulse of known voltage to this capacitor an electric charge is injected into the preamplifier. In this way the performance of the entire electronic chain was monitored at regular intervals.

An analysis of the most probable number of ADC channel counts recorded for the injection of a known charge can be used to validate the assumption of linearity to within 1% for the equivalent energy range from 15 to 280 MeV. (Unfortunately, this procedure does not quite cover the complete range desired, but we have no reason to suspect any sudden nonlinear behaviour just below and just above the region studied.) Figure 4 shows the linearity of this relationship for a typical high gain channel.

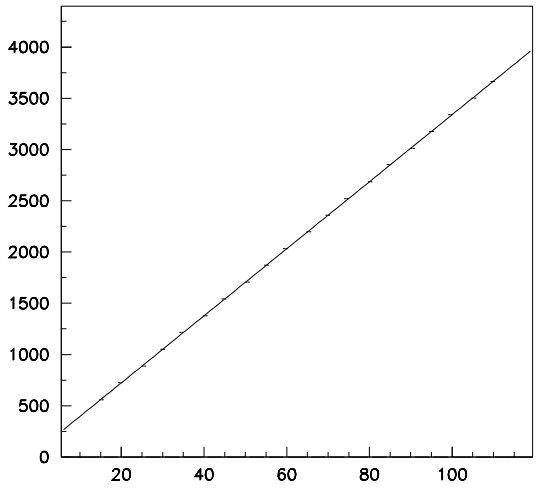

Figure 4: The relationship between injected charge in arbitrary units (abscissa) and ADC channel count (ordinate). The distribution validates the assumption of linearity between 15 and 280 MeV

3.3 Calibration using Pions

After the first period of running, the 9 inner crystals of the matrix were recalibrated with electrons. This recalibration revealed a shift of the calibration constants which could not be explained by shifts in the electronics calibration. To compensate for this drift, run-by-run corrections were made to the gain calibration for the central crystals. In this secondary calibration we use the energy loss of charged pions.

For beam momenta below 320 MeV/c, the pions can lose all of their kinetic energy and come to rest in one crystal, thus exhibiting a pronounced stop peak in the energy loss distribution. For higher beam energies, pions will leave the crystals. For a sample of pions identified by the time-of-flight system we demand that the impact point of the track extrapolated from the wire chamber on to the front face of the crystal must be more than 0.5 cm away from any crystal edge.

Due to limitations imposed by the beam profile it is only possible to calculate the calibration parameter for the central 9 crystals. A cut on the shower energy deposited in neighbouring crystals enhances the pion stop peak with respect to pions interacting hadronically.

Figure 5 shows the spectrum of pedestal subtracted ADC counts for the 215 MeV/c π^- data. The distribution has been made for a high gain channel connected to a central crystal. The pion stop peak is clearly visible on the broad background up to the beam energy.

Knowing the beam momentum and energy loss in the scintillators in front of the crystals, the peak ionisation energy was calculated for simulated negative pions at various momenta. All processes of nuclear interaction were switched off. For stopped pions of momenta 100 MeV/c, 135 MeV/c, 215 MeV/c and 320 MeV/c the peaks were calculated as being 24.2 MeV, 49.2 MeV, 112.9 MeV and 206.2 MeV respectively. Comparing the most probable ADC counts to these energies at the 3 lowest beam momenta shows an excess energy of 9 MeV, about half of which can be explained as the energy of photons emitted when the pion is bound in a pionic atom to a Cs, I, or Tl nucleus.

To adjust the recalibrated crystals to the outer ones where the initial calibration had to be retained, all calibration constants were multiplied by a factor 0.996, which has been determined at one channel in run 289 providing high statistical precision. The runs at beam momenta of 135 MeV/c and 215

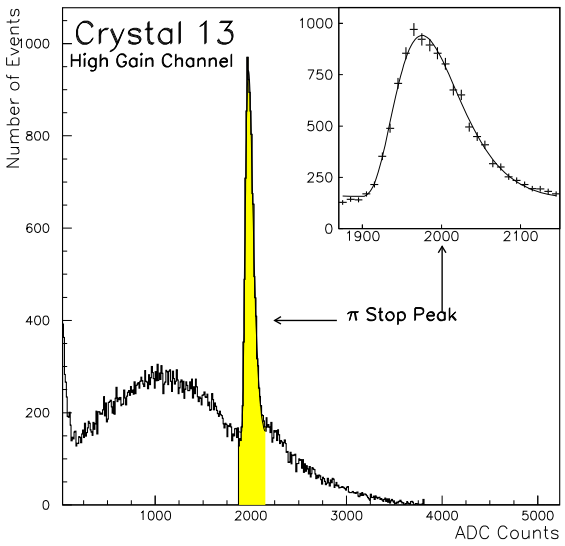

Figure 5: Pedestal subtracted ADC counts for a sample of 215 MeV/c π^- incident on the front face of the crystal. The curve represents the result of a fit to the pion stop peak. The shaded area is the limited region over which the fit was performed.

MeV/c were recalibrated with pions as described here; for runs with beam momenta of 100 MeV/c and 320 MeV/c the calibration constants were taken from recalibrated neighbouring runs. For runs with 405 MeV/c momentum, the crystals were calibrated relative to each other with pions; in this case the calibration was fixed to one photodiode which was taken as stable.

Comparing the calibration constants from the initial electron calibration and pion calibration it was found that the two methods agreed to within 0.5%. Augmenting the initial electron calibration with run-by-run pion calibration improved the energy resolution of the electrons.

4 Noise Effects

4.1 Pedestal Runs

Electronic noise and pedestal drifts were monitored using pedestal runs recorded every 3 minutes as part of the normal data flow. These runs of 100 contiguous pedestal events were triggered by an internal 1 kHz clock. Any pedestal event triggered within 20 μs after the arrival of a beam particle was vetoed as an overlap event.

Figure 6 shows the evolution of the pedestal value for a typical single readout channel over many data runs during a 5 day period. The drifts seen in this channel are mirrored in all channels, both low and high gain. Their cause is not understood.

Temperature probes within the box housing the crystals were read out every 10 s through the same ADC system as the amplifiers, and displayed drifts with many of the gross features seen in the pedestal drifts. These "temperature" drifts could not be correlated with readings from a more reliable hand-held temperature probe. They turned out to give a good short-term correction of pedestal shifts, but this was not sufficient over a long timescale. Therefore each pedestal was updated dynamically during off-line analysis using the pedestal monitoring runs. Each set of updated pedestal values is used for the following 3 minutes of beam data.

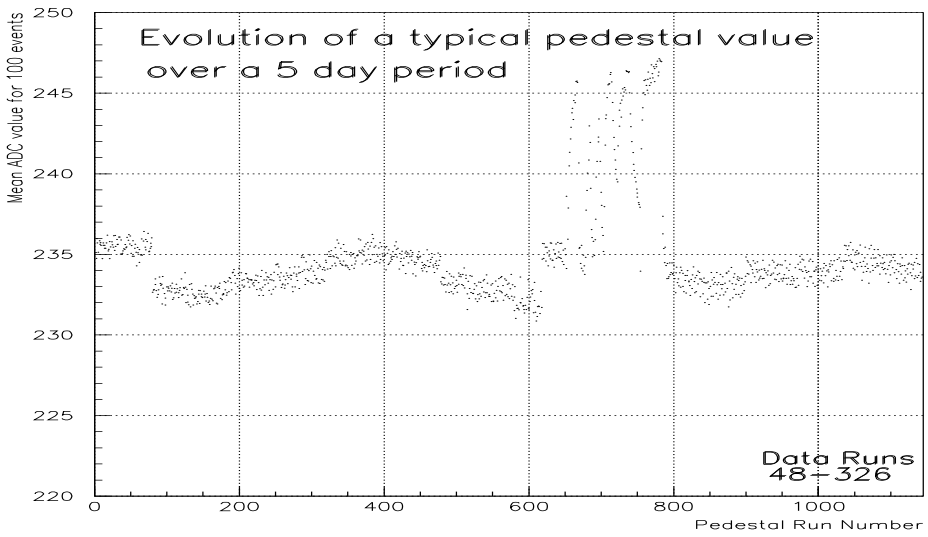

Figure 6: Evolution of a typical pedestal value (ADC counts) with run number. The period shown spans 5 days.

4.2 Beam Rate Effects

The amplifiers produce waveforms which peak $\sim 6\,\mu$s after the arrival of beam particles and exhibit a later "undershoot" which extends beyond the $20\,\mu$s veto region.

Events occuring after the veto window but during the undershoot from a previous beam particle have lower effective pedestals and correspondingly depressed peak heights.

The fraction of events affected increases with increasing beam rate. Owing to the random nature of this effect, it smears the energy distribution. The data had to be corrected for this effect, since the final design sampling ADC system will not be susceptible to this. These corrections will be presented in section 5.

4.3 Incoherent Noise

The incoherent noise in a single channel was determined by fitting the single photodiode pedestal distribution with a Gaussian plus a linear background on the low energy side for the undershoot. Typical Gaussian standard deviations of 0.5 and 5 ADC counts were obtained for the low and high gain channels, respectively. Using the individual channel gains determined in the calibration procedure (see Section 3) we can determine the equivalent noise energy for each photodiode.

The mean noise for all high gain channels was measured to be 411 keV during normal beam operation, see Figure 7, and slightly less during the beam-off runs. Owing to better light collection and to the lower capacitance of the smaller photodiodes, the wavelength shifter readout crystals had a lower mean noise of 349 keV per high gain channel (beam-on) than the 450 keV found for the direct readout crystals. The results, together with those for the low gain channels, are summarized in Table 1.

In the absence of any coherent noise, we should attain a noise of $411/\sqrt{2} = 290$ keV per crystal if the light collection and gain are the same for the two channels. The final calorimeter is expected to have about twice the light yield found here and correspondingly lower noise. This would satisfy the *BABAR* noise goal [1] of < 150 keV per crystal based on resolution requirements for the lowest energy photons of interest (~ 20 MeV).

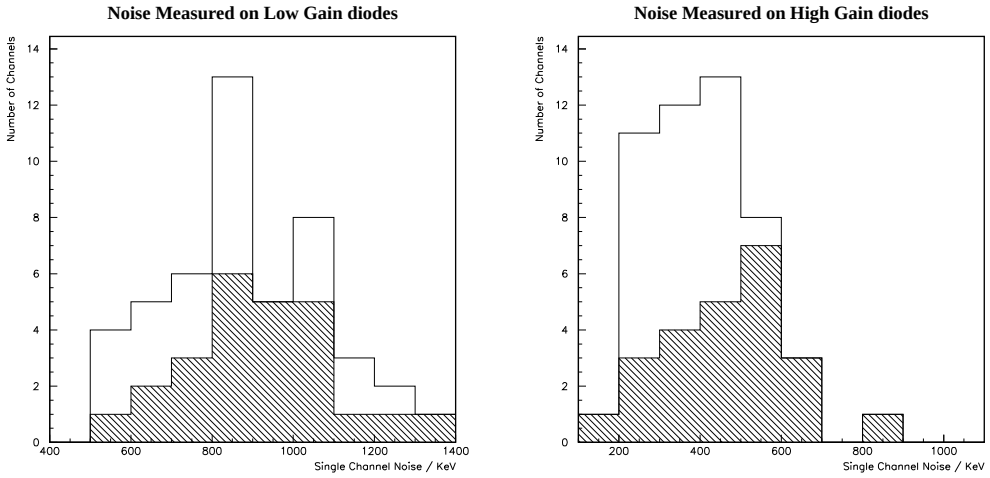

Figure 7: Single channel noise obtained from pedestal events for all low and high gain channels. The direct readout channels are shown as the hatched histograms

	Low Gain Channels Noise(keV)	High Gain Channels Noise (keV)
All	881	411
WLS	846	349
Direct	921	450

Table 1: Mean noise measured per photodiode. Data are presented in keV for wavelength shifter (WLS) and direct readouts and for both combined.

4.4 Coherent Noise

In the presence of coherent noise, the event-to-event fluctuations of pedestals about their mean values are correlated between readout channels. Figure 8 shows the noise covariance matrices for various runs, $V_{ij} = \langle (p_i - \overline{p}_i)(p_j - \overline{p}_j) \rangle$ where p_i and p_j are pedestals of channels i and j, and $\overline{p}_i$ and $\overline{p}_j$ are the corresponding mean pedestal values. Here pedestal events from typical runs were used with the "undershoot" tail removed. Covariance matrices obtained from beam-on and beam-off runs are very similar.

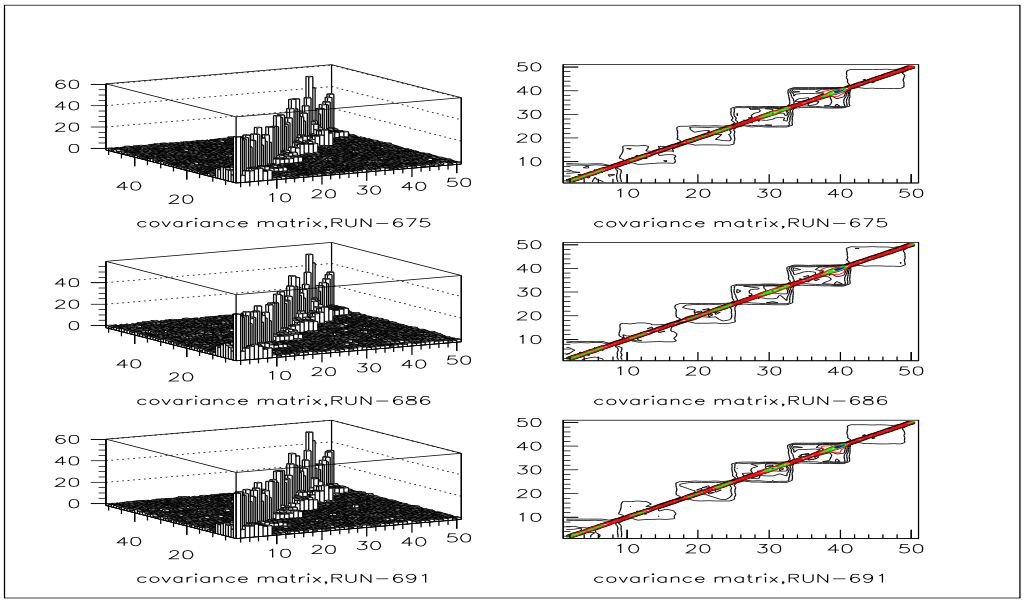

Figure 8: Covariance matrices showing correlations between crystals connected to the same receiver card.

In the absence of coherent noise only the 50 diagonal matrix elements would be non-zero, with values corresponding to the variance of the incoherent noise distributions (ADC counts). Instead, significant coherent noise is seen in six groups of eight readout channels, *i.e.* four crystals. Each of these groups of eight channels are connected to a single receiver board of the DAQ system. Readout channels connected to different receiver boards exhibit little coherent noise.

It is believed that the noise sources are the power supply Zener references located on each receiver board. This arrangement is unique to the beam test. The receiver boards will not be present in *BABAR*, and care will be taken to eliminate power supply noise from the *BABAR* calorimeter.

For two readout channels, i and j, we may define the correlation coefficient

$$C_{ij} = \frac{V_{ij}}{\sigma_i \sigma_j} = \frac{\sigma(i+j)^2 - \sigma(i)^2 - \sigma(j)^2}{2 \times \sigma(i) \times \sigma(j)}$$

as a measure of the coherent noise where $\sigma(i)$, $\sigma(j)$, and $\sigma(i+j)$ denote the widths of the pedestal distributions for channels i, j, and their sum, respectively. In the limits of purely incoherent noise and purely coherent noise C_{ij} assumes the values 0 and 1. Typical C_{ij} values of 0.15 indicate that incoherent noise is dominant for single crystals. The coherent noise contribution becomes more significant as more crystals are summed. When all crystals are summed the total noise is 3.56 MeV compared to 1.45 MeV if the 290 keV noise per crystal is added incoherently.

5 Energy Resolution

The distribution of recorded shower energies E is described by a function, which is discussed in detail in ref. [11]:

$$f(E) = \mathcal{N} \cdot (E_C - E)^{\frac{A - \ln(E_C - E)}{B}}, \tag{1}$$

with three parameters A, B and E_C, that can be transformed into the physical parameters

$$E_p = E_C - e^{(A+B)/2},$$

the energy at the peak, and

$$\mathrm{FWHM} = e^{(A+B)/2} \sinh \sqrt{B \ln 2},$$

the energy resolution defined by the full width at half maximum of the distribution. We present the relative energy resolution as

$$\frac{\sigma_E}{E} = \frac{\mathrm{FWHM}}{2.36 E_p}.$$

The energy measured by diode k of crystal i is given by

$$E_{ik} = C_{E(ik)} \cdot (\mathrm{ADC} - \mathrm{PED}),$$

The measurement of both diodes is averaged as

$$E_i = \frac{E_{i1}/\sigma^2_{Ni1} + E_{i2}/\sigma^2_{Ni2}}{1/\sigma^2_{Ni1} + 1/\sigma^2_{Ni2}}$$

which gives a modest improvement over direct addition, and has the advantage that it suppresses any measurements from defective diodes.

When measuring the energy resolution we use events where the particle has been identified as an electron by the time-of-flight system. We only use events with exactly one track seen in the wire chambers, and the angle of that track with respect to normal incidence on the face of the central crystal is required to be less than 28 mrad.

5.1 Energy Threshold

The measured energy E is a sum over all E_i in a cluster which are above a chosen threshold. The optimum single-crystal energy threshold is a compromise between using the maximum number of crystals which have contributed to the shower development and minimising the effect of electronic noise. In Table 2 we show the resolution measured for different single-crystal thresholds at different beam momenta. This indicates that under beam-test conditions the optimum threshold is close to 1.0 MeV. In the following, we define the energy of an electromagnetic shower as the sum over all crystals with energy $E_i > 1.0\,\mathrm{MeV}$. With this threshold, the average number of crystals contributing to the sum rises from $\langle n_{E>1} \rangle = 4.8$ at $100\,\mathrm{MeV}/c$ to $\langle n_{E>1} \rangle = 9.6$ at $405\,\mathrm{MeV}/c$.

Reducing the threshold from 1.0 MeV to 0.5 MeV at $215\,\mathrm{MeV}/c$ increases the average number of crystals in a cluster from 7 to 10 and the peak energy by 1 MeV as shown in Fig. 9.

5.2 Energy Resolution and Impact Position

The distribution of electron energy deposition, for four different impact regions, are shown in Figures 10 and 11 for $215\,\mathrm{MeV}/c$ and $405\,\mathrm{MeV}/c$ respectively. By using four non-overlapping regions we can separate the effect of

Table 2: Uncorrected energy resolutions σ_E/E_0 versus single-crystal threshold.

P_{beam} [MeV/c]	100	135	215	320	405
$E_i > 0.0\,\mathrm{MeV}$	3.08%	2.87%	2.08%	2.11%	1.93%
$E_i > 0.5\,\mathrm{MeV}$	2.80%	2.36%	2.16%	2.25%	1.76%
$E_i > 0.8\,\mathrm{MeV}$	2.80%	2.12%	1.95%	2.22%	1.66%
$E_i > 1.0\,\mathrm{MeV}$	2.65%	2.24%	1.89%	2.09%	1.82%
$E_i > 1.2\,\mathrm{MeV}$	2.90%	2.26%	2.18%	2.29%	1.94%

position-dependent peak shift and remove any dependence of rate variations across the face of the crystals on the measured resolution.

The four regions as shown in Fig. 10 are periodically repeated to cover the entire area, and are defined as

- x-edge (xe): $\pm 1\,\mathrm{cm}$ within the vertical crystal boundary line,
- centre (ce): $3 \times 4\,\mathrm{cm}^2$ central impact area,
- corner (co): $\pm 1\,\mathrm{cm}$ in each direction from a corner, where 4 crystals meet, and
- y-edge (ye): $\pm 1\,\mathrm{cm}$ within the horizontal boundary line.

We determine the resolution σ_E in two ways. In the first, we use Equation 1 to perform a fit within a limited range around the peak. Statistical errors on the fit parameters are small. However, variations in the width parameter, due to differences in shape between the fit function and the data, which are observed when the fit interval is changed, limit the precision. In the second method the histogram containing the distribution is smoothed before determining the full height and then the full width at half height. In both cases the difference between a resolution extracted from a histogram "by-hand" and using one of the automated techniques is of the order of $\pm 0.10\%$ absolute. The results are summarised in Table 3. These "raw" results include the effect of the beam related undershoots. This effect can be subtracted from the data, as will be described in the following, and the corrected results are presented in the same table.

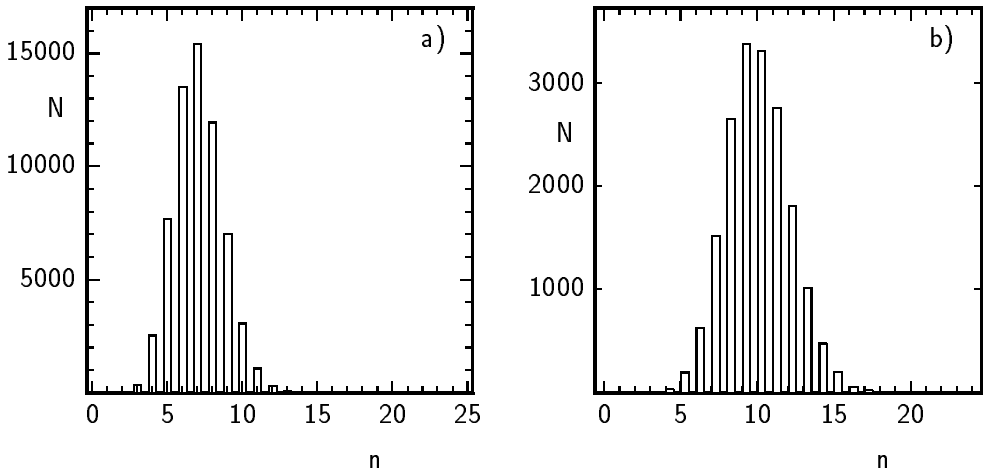

Figure 9: Number of crystals n with $E_i > 1.0\,\mathrm{MeV}$ **(a)** and $E_i > 0.5\,\mathrm{MeV}$ **(b)** contributing to electron showers at 215 MeV beam energy. Mean and rms are $\langle n_{E>0.5} \rangle = 10.0$, $\sigma = 2.1$ and $\langle n_{E>1} \rangle = 7.1$, $\sigma = 1.6$. In our Monte Carlo simulation without noise, these averages are $\langle n_{E>0.5} \rangle = 9.1$ and $\langle n_{E>1} \rangle = 7.3$.

The overall resolution is given by averaging in quadrature, weighted by the area covered, as

$$\bar{\sigma} = \sqrt{\frac{8\sigma_{xe}^2 + 12\sigma_{ce}^2 + 4\sigma_{co}^2 + 6\sigma_{ye}^2}{30}} \tag{2}$$

5.3 Undershoot Corrections

The resolutions at 215 MeV are $\sigma_E/E = 2.8\%$ and $\sigma_E/E = 2.3\%$ for runs 289–297 and run 462 respectively. The differences between the values are attributed to the beam related undershoots and indicate the care needed in extracting resolutions. To make meaningful comparisons between the Monte Carlo model and the data, Monte Carlo events have first been simulated with no intrinsic noise. Individual pedestal events, recorded at the test beam, are then "added" to each simulated event. In this way Gaussian noise, coherent noise between different parts of the test beam apparatus and undershoot effects are simulated in one step. In all cases where comparisons are made between data and the modified Monte Carlo, the pedestal events have been taken from the same runs as the data events. To remove short term variations

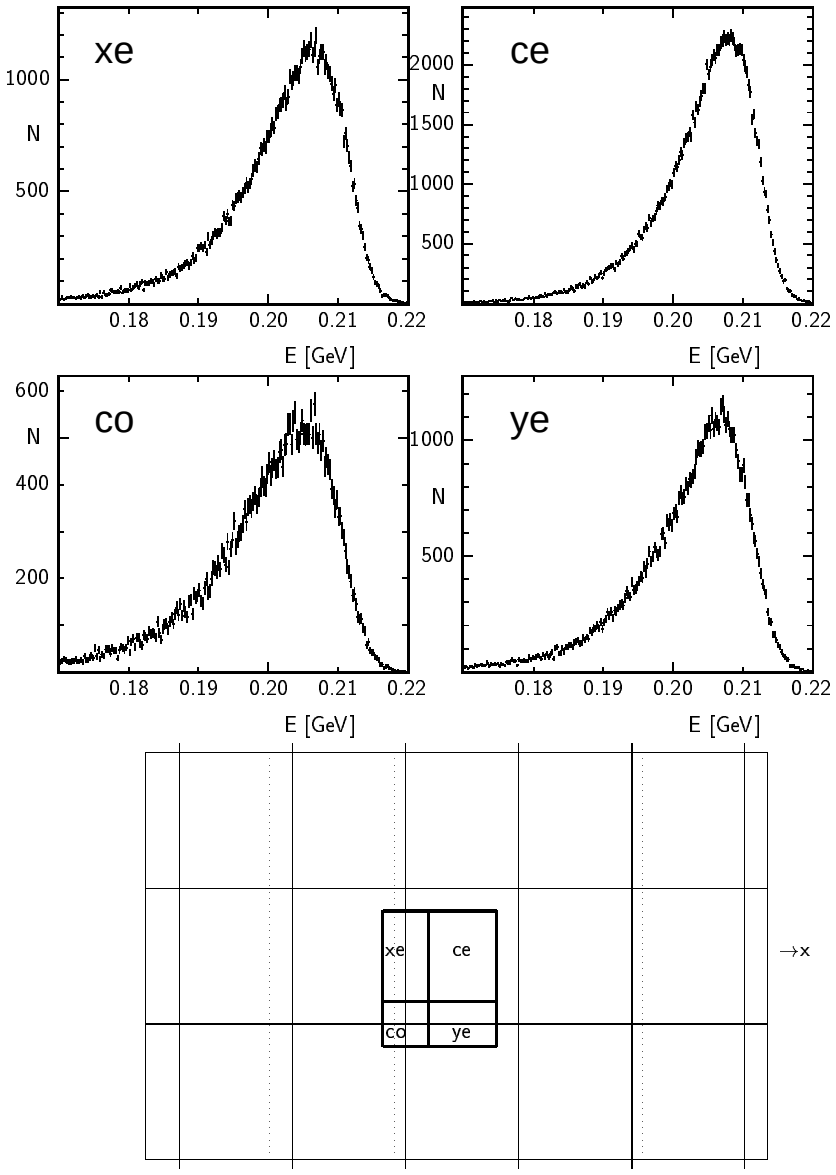

Figure 10: Measured energy depositions for electrons at 215 MeV/c beam momentum (runs 289, 292, 294 and 297). The distributions are shown for four different impact fields on the central crystal. These fields are illustrated in the lower figure. The solid and dotted lines show the crystal edges at the front and rear, respectively, of the crystal matrix.

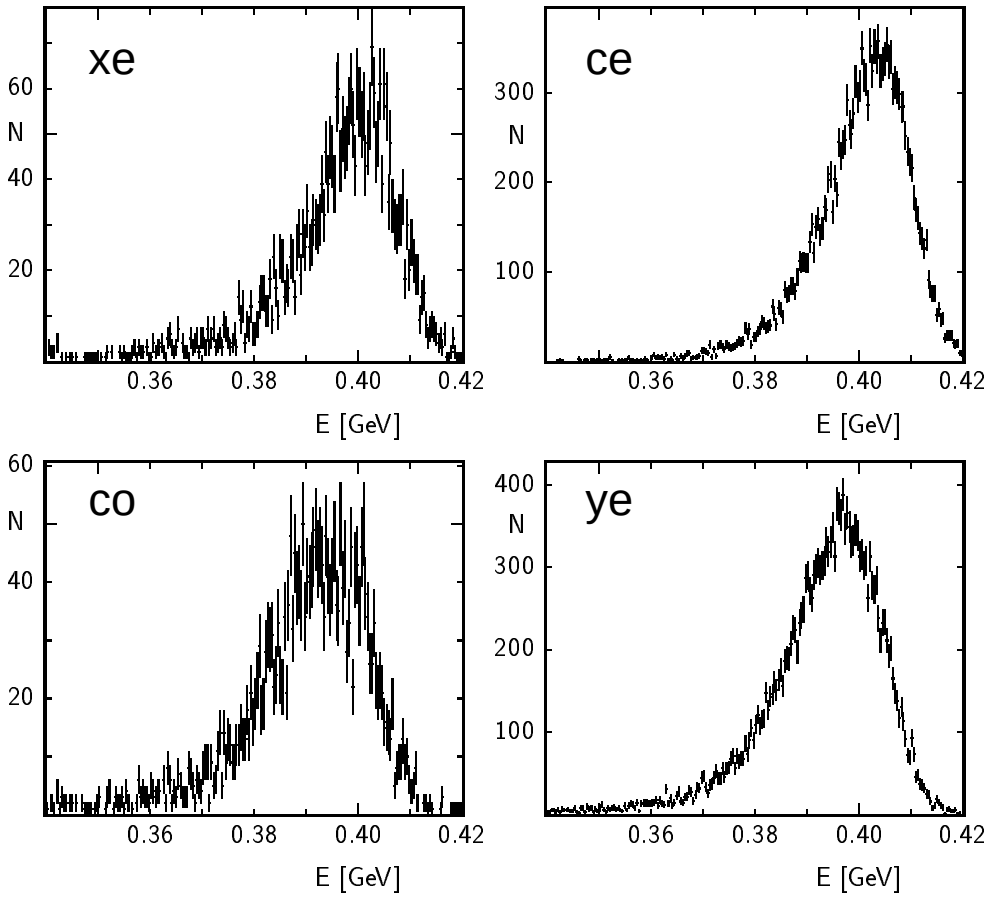

Figure 11: Energy distributions at 405 MeV/c beam momentum (runs 429, 438, 441, 444, 447 and 450) for the 4 impact fields of the central crystal, as shown in Fig. 10.

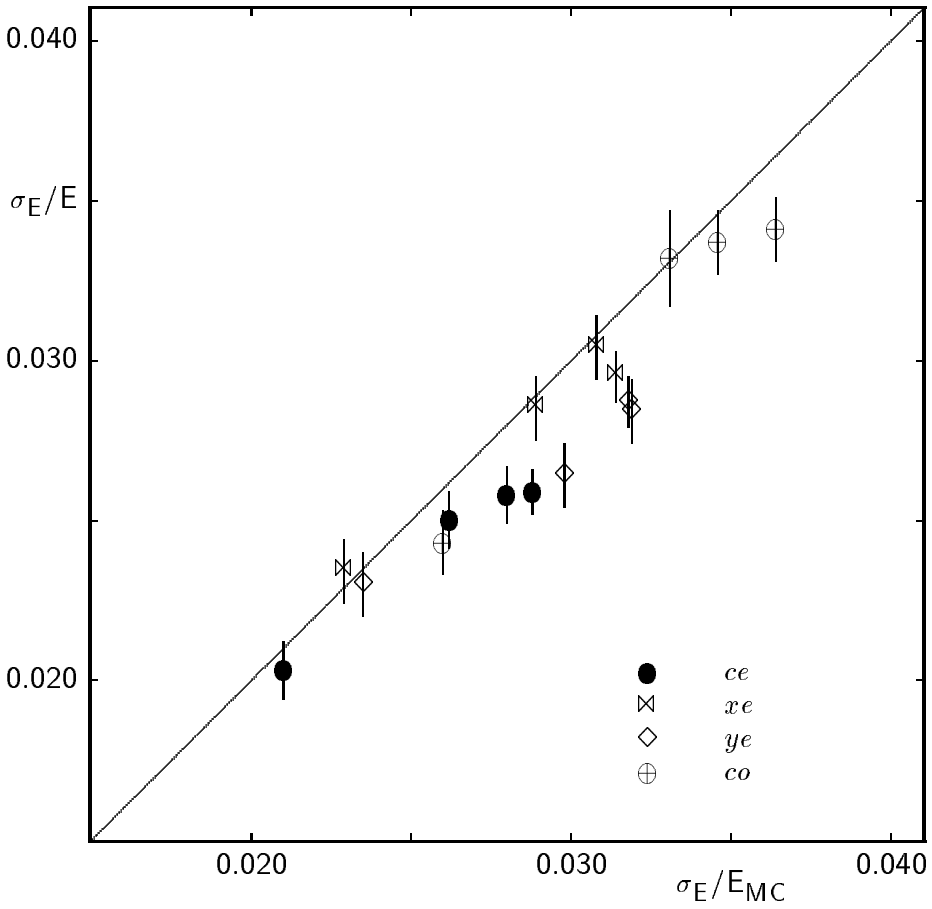

Figure 12: Energy resolution of 215 MeV/c data versus MC prediction using weighted pedestals as noise simulation, for the fields ce : ●, xe: ⋈, ye : ◇, and co : ⊕. The solid line is the identity, i.e. the MC predictions.

in the undershoot, caused by the varying beam intensity within a data run, care has been taken to weight each Monte Carlo event with a weight proportional to the number of electrons identified between successive pedestal runs.

In Fig. 12 we show a comparison of four 215 MeV/c data samples for the four impact fields. Each data point is compared with the appropriate Monte Carlo prediction which includes the contribution from electronic noise (coherent and incoherent) and undershoots taken from the appropriate pedestal run. The four samples are: run 462, runs 814–854, and runs 289–297, split into a low-rate and a high-rate sample. The solid line represents equality between data and the Monte Carlo predictions. Each groups of four points associated with one impact point shows a tendency to fall below this line. The amount by which they fall below increases with beam related undershoots. Assuming a linear correction and a common slope for each data sample, 0.75 of the Monte Carlo correction fit the data best.

In a second analysis of energy resolution, Gaussian noise (including the coherent effects) is added to the "no-noise" Monte Carlo events. The difference between the fully simulated events (including undershoot) and those with Gaussian noise alone is scaled with the factor 0.75 and then subtracted from the data, to correct the data for the undershoot effect. The resolutions measured using this technique are presented in Table 3.

Table 3: Energy resolutions and peak positions at various energies for the 4 impact fields of Fig. 10, with a $3 \times 4\text{cm}^2$ central region, two $2 \times 3\text{cm}^2$ vertical edges, two $2 \times 4\text{cm}^2$ horizontal edges and four $2 \times 2\text{cm}^2$ corners. The "raw" results include the effect of the beam related undershoot. The corrected results have had this effect removed. If a corrected peak energy is not shown, it is the same, within the errors, as the raw value.

Beam	Runs	Field	Peak Energy (MeV)		Resolution (%)	
MeV/c			Raw	Corrected	Raw	Corr.
215	289-297	xe	206.4 ± 0.4	208.0 ± 0.4	3.0 ± 0.1	2.2 ± 0.1
		ce	208.0 ± 0.3	208.9 ± 0.3	2.5 ± 0.1	1.9 ± 0.1
		co	205.5 ± 0.5	206.0 ± 0.5	3.4 ± 0.1	2.6 ± 0.1
		ye	206.9 ± 0.3	208.4 ± 0.3	2.8 ± 0.1	2.0 ± 0.1
	462	xe	206.2 ± 0.4	208.8 ± 0.4	2.4 ± 0.1	2.2 ± 0.1
		ce	209.7 ± 0.2	209.7 ± 0.2	2.0 ± 0.1	1.9 ± 0.1
		co	207.4 ± 0.5	207.4 ± 0.5	2.4 ± 0.1	2.2 ± 0.1
		ye	208.0 ± 0.4	208.0 ± 0.4	2.3 ± 0.1	2.1 ± 0.1
100	453-459	xe	97.7 ± 0.3		3.0 ± 0.1	2.8 ± 0.1
		ce	98.0 ± 0.3		2.8 ± 0.1	2.7 ± 0.1
		co	96.7 ± 0.4		3.3 ± 0.1	3.1 ± 0.1
		ye	98.0 ± 0.3		3.0 ± 0.1	2.8 ± 0.1
135	358–364	xe	131.4 ± 0.4		2.7 ± 0.1	2.6 ± 0.1
		ce	131.4 ± 0.3		2.5 ± 0.1	2.4 ± 0.1
		co	130.2 ± 0.5		3.0 ± 0.1	2.9 ± 0.1
		ye	131.0 ± 0.3		2.7 ± 0.1	2.6 ± 0.1
320	339–354	xe	310 ± 1		2.5 ± 0.2	2.3 ± 0.2
		ce	313 ± 1		1.8 ± 0.1	1.7 ± 0.1
		co	308 ± 1		2.2 ± 0.2	2.0 ± 0.2
		ye	310 ± 1		2.0 ± 0.1	1.8 ± 0.1
405	429–450	xe	399 ± 1		2.0 ± 0.1	1.9 ± 0.1
		ce	404 ± 1		1.8 ± 0.1	1.7 ± 0.1
		co	392 ± 1		2.5 ± 0.2	2.4 ± 0.2
		ye	397 ± 1		2.2 ± 0.1	2.1 ± 0.1

5.4 Energy Resolution Results

In Fig. 13 we show the corrected electron energy resolutions measured as a function of beam momentum. They include noise but are corrected for the undershoot effects. For comparison, we also show the Monte Carlo simulation including coherent and incoherent noise. The results are listed in Table 4.

Table 4: Energy resolutions, corrected for uniform illumination and no undershoots. The errors are systematic. The asymmetric errors indicate that a naïve Monte Carlo correction for undershoots would have resulted in lower resolution numbers.

$E = 100\,\mathrm{MeV}$	runs 453 ..	$(2.82 \pm {}^{0.10}_{0.15})\%$
$E = 135\,\mathrm{MeV}$	runs 358 ..	$(2.56 \pm {}^{0.10}_{0.12})\%$
$E = 215\,\mathrm{MeV}$	runs 289 .., low rate	$(2.13 \pm {}^{0.10}_{0.15})\%$
	runs 289 .., high rate	$(2.12 \pm {}^{0.10}_{0.15})\%$
	run 462	$(2.06 \pm 0.10)\%$
	runs 814 ..	$(2.03 \pm 0.10)\%$
$E = 320\,\mathrm{MeV}$	runs 339 ..	$(1.92 \pm {}^{0.10}_{0.15})\%$
$E = 405\,\mathrm{MeV}$	runs 429 ..	$(1.92 \pm {}^{0.10}_{0.14})\%$

5.5 Staggered Crystal Configuration

An important issue is the deterioration of calorimeter resolution due to the staggering. The maximum effect is expected at the end of the barrel in the *BABAR* calorimeter. This extreme situation was investigated in the test beam by staggering the 3 central columns with 10 cm offset along the beam direction, as shown in Fig. 14. At 215 MeV, this arrangement gives a resolution of $(3.20 \pm 0.10)\%$ after averaging over impact positions and correcting for undershoots [12]. This increase by a factor of 1.5 is mainly due to fluctuations in side leakage. The longitudinal shower development has its maximum energy deposition at 5 cm from the front face.

The Monte Carlo simulation resulted in a similar but slightly lower value for the relative energy resolution, $(2.93 \pm 0.10)\%$. This sets the scale for the reliability of shower simulation, which is expected to improve with higher

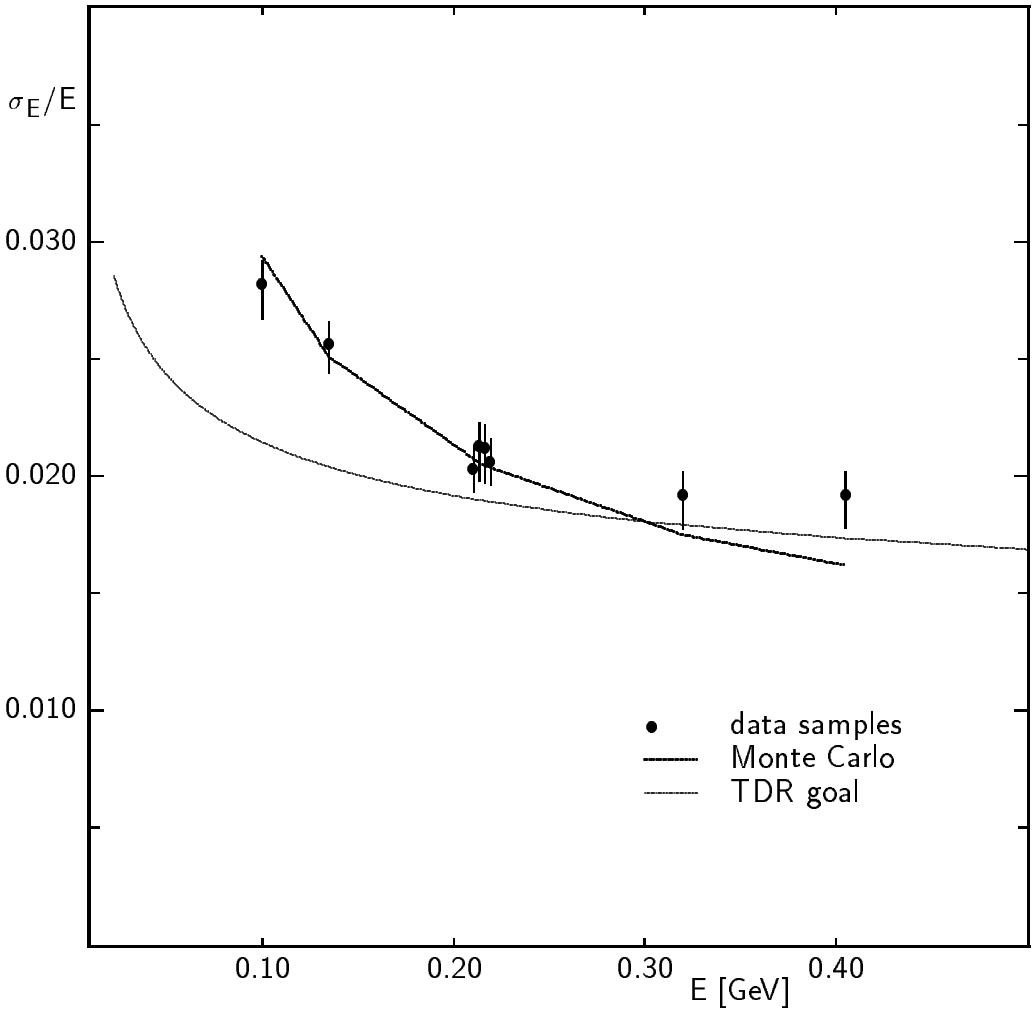

Figure 13: Energy resolution for electrons as a function of beam momentum. The solid points are the data corrected for beam related undershoot (described in the text). The Monte Carlo prediction including the electronic noise measured at PSI is given as a solid line. The thin line is the expectation from a simulation of the BABAR detector setup at 90° polar angle and without noise [1].

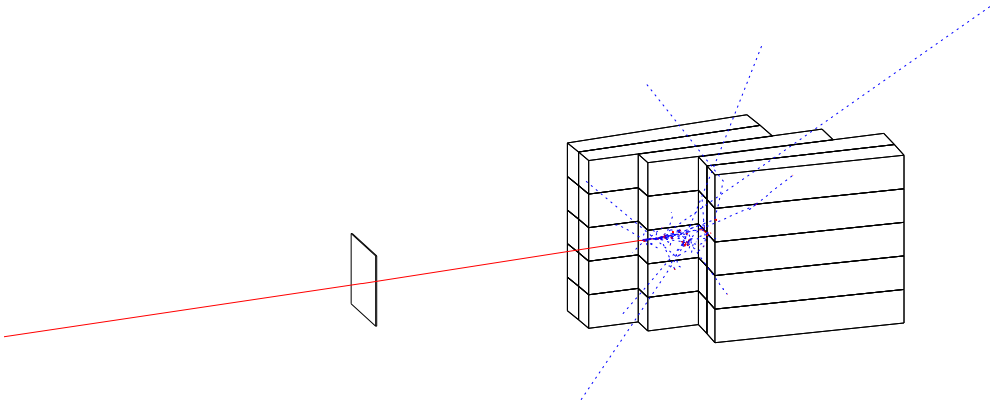

Figure 14: The experimental configuration with staggered crystals. The offset of the front faces is 10 cm.

energy, where it predicts still an increase by a factor of 1.5 in the width of 1 GeV electron energy and a shower maximum 8 cm away from the front face.

Small scale staggering, on the other hand, has no effect on resolution. This can be inferred from a Monte Carlo study with an offset of 1 cm of the front faces. This small offset didn't change the resolution at all within statistical precision [12].

6 Position Resolution

In the absence of multiple scattering the point of impact of a charged particle on the front face of the crystal matrix ($(x, y)_{track}$) can be determined, to a high degree of accuracy, from the wire chamber hits. The position of the shower $(x, y)_{\text{shower}}$ can be calculated by considering the centre of gravity of the three columns and of the three rows centred on the crystal with the maximum recorded energy. The measurement becomes more accurate as the energy of the incident particle increases and more significant energy (with respect to the noise) is deposited in the 8 crystals surrounding the central crystal.

In Fig. 15 we show the difference in the x co-ordinates determined from

the point of impact derived from the wire chambers and the shower start determined from the centre-of-gravity for two beam momenta. The offset from zero reflects an offset of the position of the wire chambers with respect to the crystal stack.

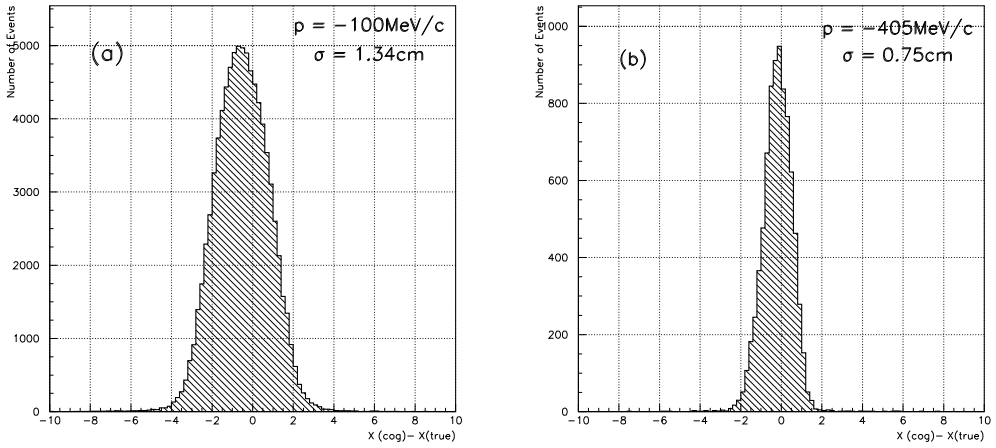

Figure 15: Position Resolution ($X_{\rm COG} - X_{\rm true}$) measured at (a) 100 and (b) 405 MeV/c. No account has been taken for the non-uniform illumination across the face of the crystal.

Because the energy leaking into the eight crystals surrounding the point of impact is a slowly varying function of the distance of the impact position from the centre of the central crystal, it is possible to improve the naïve centre-of-gravity result. This is achieved by applying an event-by-event position dependent correction to the centre-of-gravity result to give the corrected-centre-of-gravity result. The correction ($\delta(X) = \langle X_{\rm true} - X_{\rm COG} \rangle$) is measured in twelve X bins across the face of the crystal to give $X_{\rm corr} = X_{\rm COG} + \delta(X)$. A different correction function is determined for each beam momentum. The "true" shower position (X_{true}) is taken to be X_{track}.

However, at PSI, as the beam energy is increased the beam profile becomes narrower until at 405 MeV/c the profile is concentrated in the centre of the central crystal. As the correction function has its maximum value around half way between the centre of the face and the edge, without uniform illumination across the face no improvement can be measured for all but the lowest momenta.

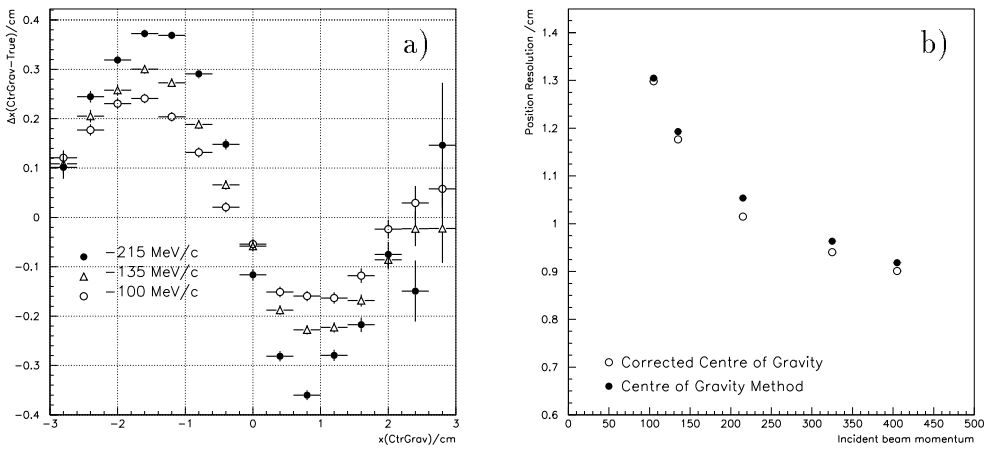

Figure 16: (a) Position dependent correction obtained from Monte Carlo simulation which can be applied to the centre-of-gravity determination. (b) Improvement in position resolution as determined by this simulation.

In Fig. 16a we show the correction applied to the centre-of-gravity for three beam momenta. The wire chambers offset mentioned above is also seen in this plot. Also shown in Fig. 16b is the improvement gained in using the corrected centre-of-gravity. These results have been obtained with a Monte Carlo simulation which has been generated with uniform illumination across the face of the crystal.

In Fig. 17 we show the measured position resolution as a function of beam momentum. The centre-of-gravity result is shown for all momenta but the corrected result is only shown for the lowest three beam momenta. The results are presented with the absolute value (left-hand scale in cm) and in angular measure (right-hand scale) for a calorimeter radius of 90cm (barrel radius). All results have been corrected for uniform illumination. Also shown is target position resolution of *BABAR* [1].

7 Hadronic Showers

It has been suggested for some time that the hadronic shower simulation code FLUKA [13] provides better agreement with low energy pion energy deposition spectra than does the GHEISHA code [14]. To allow this effect to be

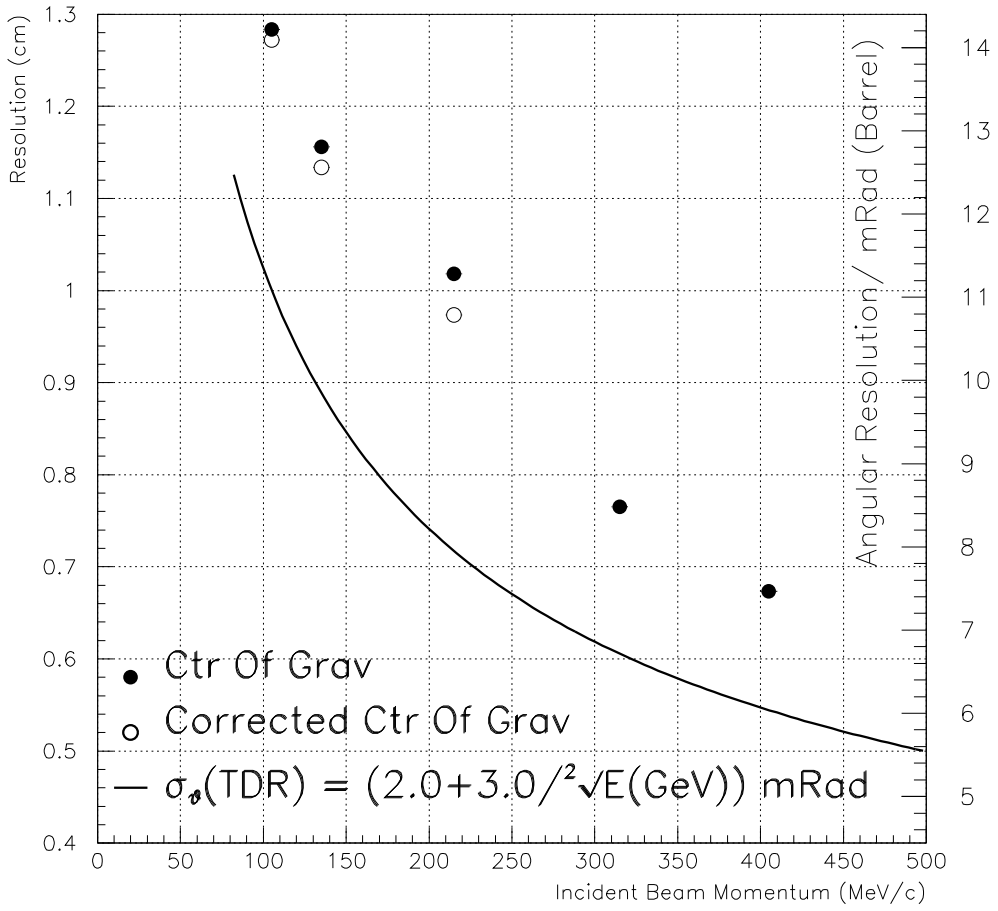

Figure 17: Position Resolution (RMS) as obtained from the test beam data. The solid curve shows the expectation from ref. [1].

studied some data were taken with positive beam, in addition to the negative beam data used in the other studies. The beam particles were a mixture of electrons, muons, pions and (for positive beams) protons. The pions were selected from the data by the time of flight, requiring a pion probability of over 1%. The deposited energy spectra for pions of the indicated polarity and momentum are shown in Fig. 18 along with predictions from the FLUKA and GHEISHA simulations. At 215/c MeV FLUKA fits the data better at the upper shoulder of the peak whilst GHEISHA does better at the lower shoulder. For 405/c MeV negative pions both programs do equally badly away from the peak, although the deviations are different. A clear distinction is shown in the 405 MeV/c positive pion data where FLUKA shows better agreement than GHEISHA. What is clear is that FLUKA does indeed provide, overall, a more adequate description of the data than GHEISHA, although neither matches the data perfectly. More details can be found in ref. [15].

8 Conclusions

The test beam experiment for the *BABAR* electromagnetic calorimeter at PSI produced several interesting results which were of importance for the final design of the calorimeter.

- The energy resolution for electrons in a 5×5 matrix of CsI(Tl) crystals, each one of 36 cm length and $5 \times 6\,\mathrm{cm}^2$ front area, was determined at five beam momenta between 100 and 405 MeV/c; at 215 MeV/c it has a RMS value of 2.1%.

- The energy resolution and its momentum dependence are in very good agreement with a Monte Carlo simulation for the test setup geometry.

- Above 200 MeV/c, the energy resolution is in very good agreement with the target resolution for the calorimeter in the *BABAR* experiment.

- The position resolution in the test beam, also measured at all five momenta, 1.0 cm RMS at 215 MeV/c, is slightly higher than the *BABAR* target, but was based only on a center-of-gravity method with one correction.

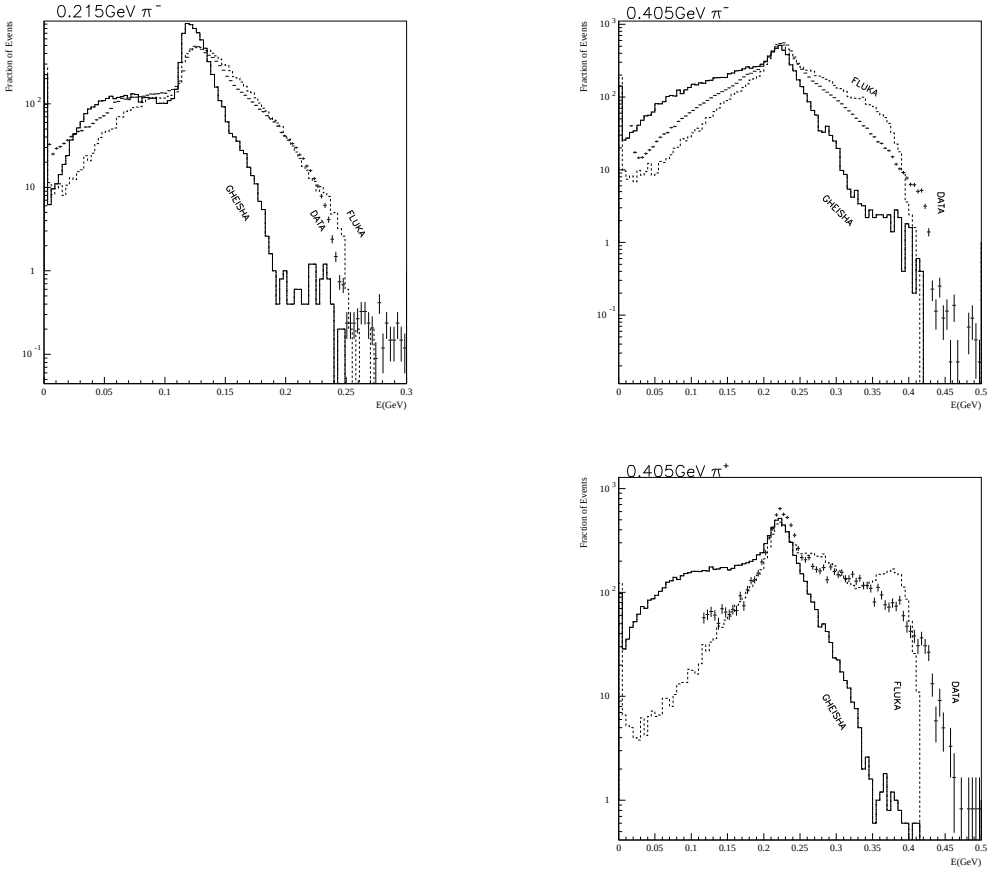

Figure 18: Data and Monte Carlo predictions for showering negative and positive pions.

- The readout electronics for the photodiodes of the crystals showed a non-negligible coherent noise which should be much lower in the *BABAR* experiment.

- The light output of the crystals depends critically on details of the coupling between crystals and diodes, and the test coupling boxes showed surprises leading to a corrected design later.

- Calibration changes, both in pedestals and gains, showed the necessity for permanent and efficient monitoring in the final *BABAR* calorimeter. In the test beam setup, stopped pions were an excellent tool for monitoring the changes.

9 Acknowledgements

We are extremely grateful to the staff at the Paul Scherrer Institute, particularly T. Flügel, K. Gabathuler, D. Renker and H. Walter, for their help and support, and for providing us with beam-time.

We acknowledge financial support from the Bundesministerium für Bildung, Wissenschaft, Forschung und Technologie, Germany, under contract 06DD558I, the U K Particle Physics and Astronomy Research Council, and the U.S. Department of Energy under contract DE-AC03-76SF00515.

References

[1] The *BABAR* Technical Design Report, SLAC-R-95-457 (1995)

[2] Users' Guide: Accelerator Facilities, ed. H. C. Walter et al., PSI, Villigen, Switzerland (1994)

[3] R. Bernet et al., *BABAR* Note 325 (1996)

[4] P. D. Dauncey and N.I.Geddes: The DAQ system for the *BABAR* Calorimeter beamtest. *BABAR* note 282 (1996)

[5] P. D. Dauncey: BTANA and BTSIM; Offline software for the *BABAR* Calorimeter beamtest. *BABAR* note 283 (1996)

[6] J. Brose et al., *Optimization of photodiode readout of CsI(Tl) crystals* *BABAR* Note 242 (1995).

[7] J. Brose, G. Dahlinger, K. R. Schubert, TUD-IKTP/98-01, accepted for publication in Nucl. Instr. and Meth. A.

[8] C. Jessop et al., *Development of the front end readout for the BABAR CsI(Tl) calorimeter*
BABAR Note 216 (1995).
C. Jessop, *Development of direct readout for CsI(Tl) calorimeter and light yield specification for crystal vendors*
BABAR Note 270 (1995).

[9] G. Dahlinger, *Wrapping and tuning studies for large CsI crystals*
BABAR Note 241 (1996).

[10] J. Brose, G. Dahlinger and R. Waldi, *The Light Yield of CsI(Tl) crystals*
BABAR Note 320 (1996).

[11] R. Seitz, *BABAR* Note 294 (1996), and references therein.

[12] G. Dahlinger, Dr.rer.nat. thesis, TUD-IKTP/98-02, TU Dresden, Jan. 1998.

[13] P.A. Aarnio *et al.*, FLUKA user's guide. technical Report TIS-RP-190, CERN, 1987, 1990

[14] H. C. Fesefeldt, Technical Report PITHA 85-02, III Physikalisches Institut, RWTH Aachen

[15] E. Tetteh-Lartey, Ph.D. thesis, Royal Holloway and Bedford New College, University of London, Nov. 1997.